Physica Medica 40 (2017) 59–65

Contents lists available at ScienceDirect

Physica Medica

journal homepage: http://www.physicamedica.com

Original paper

Development and validation of an accurate GATE model for NeuroPET scanner

Peyman Sheikhzadeh [a,b], Hamid Sabet [c], Hossein Ghadiri [a,b], Parham Geramifar [d], Hojjat Mahani [b,e], Pardis Ghafarian [f,g], Mohammad Reza Ay [a,b,*]

[a] Department of Medical Physics and Biomedical Engineering, Tehran University of Medical Science, Tehran, Iran
[b] Research Center for Molecular and Cellular Imaging, Tehran University of Medical Sciences, Tehran, Iran
[c] Massachusetts General Hospital, Harvard Medical School, Boston, MA, USA
[d] Research Center for Nuclear Medicine, Shariati Hospital, Tehran University of Medical Sciences, Tehran, Iran
[e] Radiation Application Research School, Nuclear Science and Technology Research Institute, Tehran, Iran
[f] Chronic Respiratory Diseases Research Center, National Research Institute of Tuberculosis and Lung Diseases (NRITLD), Shahid Beheshti University of Medical Sciences, Tehran, Iran
[g] PET/CT and Cyclotron Center, Masih Daneshvari Hospital, Shahid Beheshti University of Medical Sciences, Tehran, Iran

ARTICLE INFO

Article history:
Received 23 November 2016
Received in Revised form 3 July 2017
Accepted 7 July 2017
Available online 14 July 2017

Keywords:
Brain-dedicated PET
Monte Carlo simulation
Inter detector scattering
NEMA standards

ABSTRACT

NeuroPET is a cylindrical full ring mobile PET/CT scanner for brain imaging that was developed by Photo Diagnostic Systems, Inc. The scanner has 7 modules, each with 3 × 4 detector blocks. The detectors have two layers of scintillator arrays with a half pixel pitch offset to realize two levels of depth of interaction. In this study, we evaluated the NeuroPET scanner modeled in the GATE simulation tool and analyzed the acquired data to better understand the contribution of inter-detector scattering (IDS). The results show that the average difference between simulated and measured data for a point-like source is 2.5%. The differences are 4.7% and 2.7% for NEMA line source in two data acquisition modes and 5.5% for peak NECR measurement. IDS evaluation indicated that the total fractions of the cross-layer crystal scatter (CLCS) and inter-layer crystal scatter (ILCS) events in singles detection mode are 1.98% and 7.98%, respectively. Approximately 90% of these CLCS events deposit most of their energy in the crystal layer other than the layer of first interaction. Additionally, no significant difference in ILCS fractions between the two layers (8.05% vs 7.35%) was observed. The simulation results demonstrate that ILCS events account for ~79% of the total mis-positioned events.

1. Introduction

The use of brain-dedicated positron emission tomography (PET) systems for accurate brain imaging in biomedical research has undergone rapid growth during the past decade. Due to their more favorable geometry for brain imaging, such PET scanners can simultaneously provide high sensitivity and high-resolution images, which may facilitate dynamic brain studies with higher accuracy [1].

Several brain-dedicated PET scanners with different detector designs and geometries have been developed in recent years. ECAT HRRT was one of the first systems dedicated to brain imaging, which was designed with an octagonal geometry and phoswich detector scheme [2]. The BGO-based Hamamatsu SHR-12000 scanner [3] and the GSO-based G-PET camera [4] were manufactured for use in brain imaging. AX-PET was developed based on axial arrangement of a matrix of long crystals, each read out by hybrid photon detectors on both their ends [5]. The J-PET scanner [6] was developed by using a four-layer detector to provide depth-of-interaction (DOI) information. Additionally, AMPET as a light and wearable brain PET [7], MINDView as an MR-compatible compact brain PET scanner [8], and Rainbow VHD brain and head/neck imager [9] and TRIMAGE as multi-modality PET/MR/EEG brain scanners [10] were developed in recent years to address the need for dedicated brain PET systems. More recently, Photo Diagnostic Systems manufactured NeuroPET/CT, a cylindrical full ring and mobile system [11,12].

NeuroPET's simple geometry, relative cost-effectiveness and single-side readout together with its unique features such as small footprint and mobility are well coordinated with our efforts to develop a cost-efficient brain-dedicated PET system at the National Brain Mapping Center, Tehran, Iran. It is noteworthy that

* Corresponding author at: Department of Medical Physics and Biomedical Engineering, Tehran University of Medical Sciences, Tehran, Iran.
E-mail address: mohammadreza_ay@tums.ac.ir (M.R. Ay).

http://dx.doi.org/10.1016/j.ejmp.2017.07.008
1120-1797/

NeuroPET/CT can potentially be used for animal and pediatric applications in addition to brain imaging. Its reported sensitivity is 0.79%, which is 24% greater than that of the HR+ system. The FDG patient study showed that NeuroPET/CT yielded 17% higher contrast than Siemens ECAT HR+ in the caudate nucleus and putamen [13].

In NeuroPET instrumentation, silicon photomultiplier (SiPM) and dual-layer offset crystal arrays (DLO) are used to provide two depth-of-interaction (DOI) levels. The DLO design consists of an $N \times N$ array of crystals positioned on top of a $(N + 1) \times (N + 1)$ crystal array with the same material and offset by half the crystal pitch, as shown in Fig. 1. The geometric distribution and pattern of scintillation light detected by the SiPMs is used to estimate the position of gamma-ray interactions in the detector. This configuration produces a uniform spatial resolution using the DOI information and leads to significant improvements in both packing fraction and sampling density compared with single-layer or no-offset dual-layer crystal array designs [14,15].

We modeled the NeuroPET system using GATE simulation code and performed various evaluation tests. More specifically, we investigated the effect of inter-detector scattering (IDS) on the performance metrics of the system. While this effect is more pronounced in detectors with multi-layer crystals, surprisingly, little effort has been devoted to addressing its effect.

IDS in pixelated scintillator crystal arrays, for which the incoming annihilation photons interact with more than one crystal within the same detector block, is one of the key factors that adversely affects image quality. It is well known that using crystal pixels with small cross-sections is necessary to achieve high spatial resolution, especially when a centroid event positioning estimator is used. However, IDS increases with decreasing pixel cross-sections, leading to non-negligible mis-positioning errors. IDS events contribute to a blurred background in the reconstructed image, which degrades lesion detectability and quantitative accuracy [16]. Therefore, it is important to investigate the overall contribution of IDS events and to estimate the first location of gamma-ray interaction [17]. There is a large body of research dedicated to estimating the first location of interaction in the detector volume, such as [18–21]. MC simulations are powerful tools for estimating the effect and contribution of IDS events [22]. In this study, we first developed and validated a GATE model for the NeuroPET/CT and then evaluated the performance characteristics of the scanner to assess the contribution of different types of IDS events.

2. Materials and methods

2.1. NeuroPET modeling

NeuroPET scanner characteristics: The NeuroPET has 4 detector rings with a ring diameter of 35.7 cm. The detector system comprises 7 detector modules, where each module has 3×4 detector blocks. Therefore, each ring is composed of 21 detector blocks. In each of the blocks, there are two layers of pixelated cerium-doped lutetium yttrium orthosilicate (LYSO:Ce) scintillator optically glued together. The two scintillator layers (22×22 for the outer layer and 21×21 for the inner layer) are placed with half scintillator pixel pitch offset with respect to each other

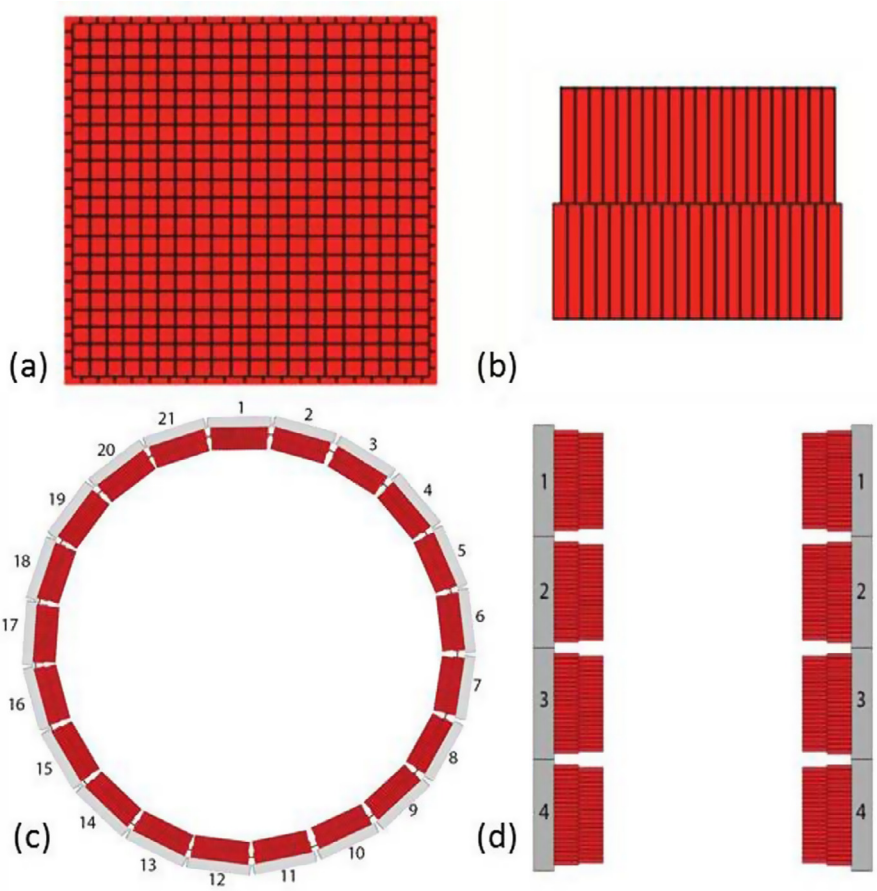

Fig. 1. Schematic drawing of the NeuroPET detector system. Top and side views of the dual-layer offset crystal block, 21×21 crystals in the inner layer and 22×22 crystals in the outer layer are shown in (a) and (b), respectively. (c) illustrates the transaxial view of NeuroPET with 21 blocks per ring and (d) shows the axial view of the NeuroPET with 4 detector rings.

(dual-layer offset configuration). Crystal pixels are $2.3 \times 2.3 \times 10\ mm^3$ in both layers. A 12×12 array of SiPMs with an external dimension of $51 \times 51\ mm^2$ is coupled to the crystal arrays to collect the scintillation light, thus realizing single-side readout and two DOI levels. It is noteworthy that while the scintillator layers are arranged in DLO configuration for DOI capability, this configuration is currently treated as a single layer with a single characteristic conversion depth in the image reconstruction code [12].

Monte Carlo model of NeuroPET: We used GATE V6.2 open source code to model the NeuroPET system [23]. This code is based on well-validated Geant4 libraries and allows for modeling time-dependent phenomena [24]. A modeled view of the NeuroPET scanner and NEMA phantoms are shown in Figs. 1 and 3.

In our simulation, photoelectric effect, Compton, Rayleigh and multiple scattering, pair production, ionization, non-collinearity, positron range and radioactive decay are considered. Optical coupling of the crystals with the SiPM arrays, as well as the light transport in the crystals, were not modeled in this work.

We used the "digitizer" modules in GATE to simulate the electronic response of the detector. In this step, the charged particle and the photon interactions are converted into energy bins, detection positions, and coincidence events. Each module of the digitizer models a portion of the signal processing chain of the scanner. The layout of the NeuroPET digitizer modules is shown in Fig. 2. The chain starts with "hits" and "adder" modules, where "hits" generate visible photons from interactions of 511 keV photons with the detector crystals, and "adder" modules transform the energy deposition by a photon or particle to a "pulse". A readout module is associated with the volume that integrates the results of the adder module. We set the detector energy resolution to 18% FWHM in the energy resolution module and used 32,000 photons/MeV light yield for LYSO:Ce crystal. The time resolution module introduces Gaussian temporal blurring. We applied 3 ns FWHM time resolution, which is similar to reported values when using similar detector configurations [14]. However, changing this value does not significantly affect the results, as the NeuroPET/CT and small-bore PET systems cannot use time-of-flight information with the current hardware technologies. In addition, we found that a quantum efficiency (QE) of 80% as a free and varied scaling factor [25,26] matches the results of the experimental values. This parameter is applied to individual events within the blocks in the digitizer chain [26]. Two "dead-time" modules were applied: the first module was applied on the block level with a value of 400 ns (paralyzable), as suggested in the NeuroPET system evaluation report [12], and a second dead time module with a value of 120 ns (non-paralyzable) was applied to account for the multiplexer processing of the single events at the module level [26]. For consistency with the scanner's experimental reports [12,13], we investigated two energy windows of 400–650 keV and 350–700 keV, and two coincidence windows of 7 and 10 ns as "tight cuts" and "loose cuts". Two values for maximum ring difference (MRD) as the axial range of the allowable coincidence events in 3D data acquisition mode were used in the simulations: 22 cm, which equals the length of the axial FOV (AFOV), and 11 cm, which is half the AFOV. We used ROOT and ASCII output to analyze the results.

2.2. Validation

Model verification: We verified the correctness of the NeuroPET model by plotting the coordinates of the detected gamma-ray photons in both the axial and the transaxial directions as a response to a point source at the FOV center similar to [27].

We performed three simulations to validate the NeuroPET scanner model: 1) point source sensitivity, 2) line source sensitivity in two acquisition modes, and 3) noise equivalent count rate (NECR). The results were evaluated and compared with the manufacturer's datasheet, as well as those reported in the literature [11–13].

Point source sensitivity: We modeled a point-like F-18 source with a 2-mm diameter surrounded by a 10-mm-thick plastic wall. The source activity and acquisition time were 10 μCi (3.7 MBq) and 1 s, respectively. Point source sensitivity is defined as the fraction of 511 keV true coincidence photon events detected for a point source with a given activity placed in the center of FOV. For absolute point source sensitivity, the branching ratio of F-18 (0.967) must be taken into account [28]. An energy threshold of 350 keV and a 7-ns coincidence window were selected for this simulation.

Line source sensitivity: Following the NEMA 2007 and 2012 protocols [29], we simulated a 700-mm-long polyethylene tube with a 2-mm inner diameter and a 3.2-mm outer diameter filled with F-18. Five concentric aluminum tubes, each 700 mm long, with outer

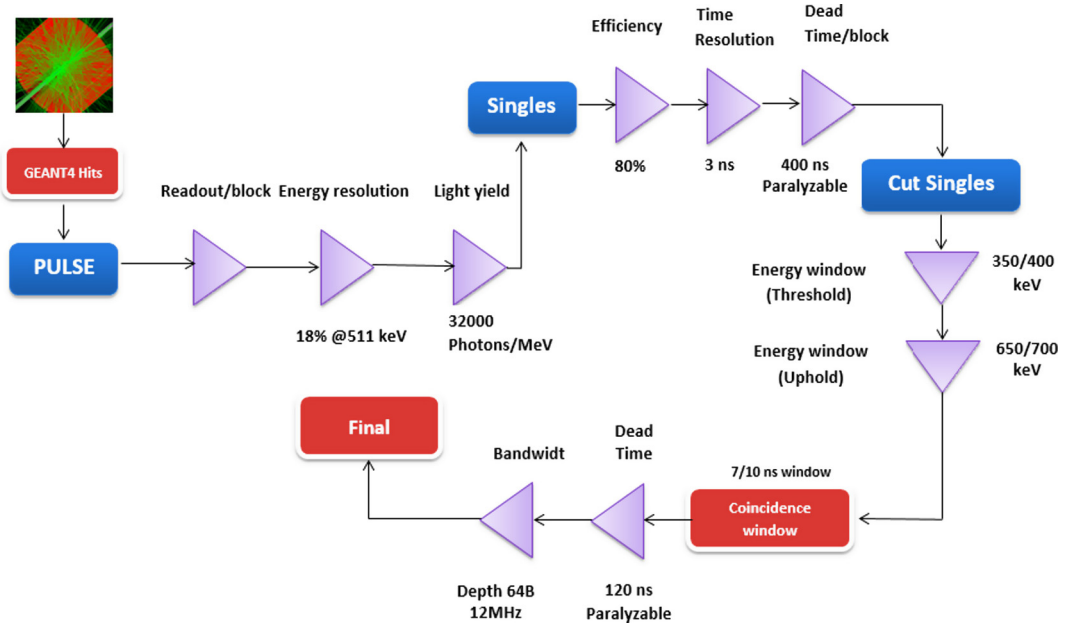

Fig. 2. Schematic of the digitizer model of the NeuroPET scanner.

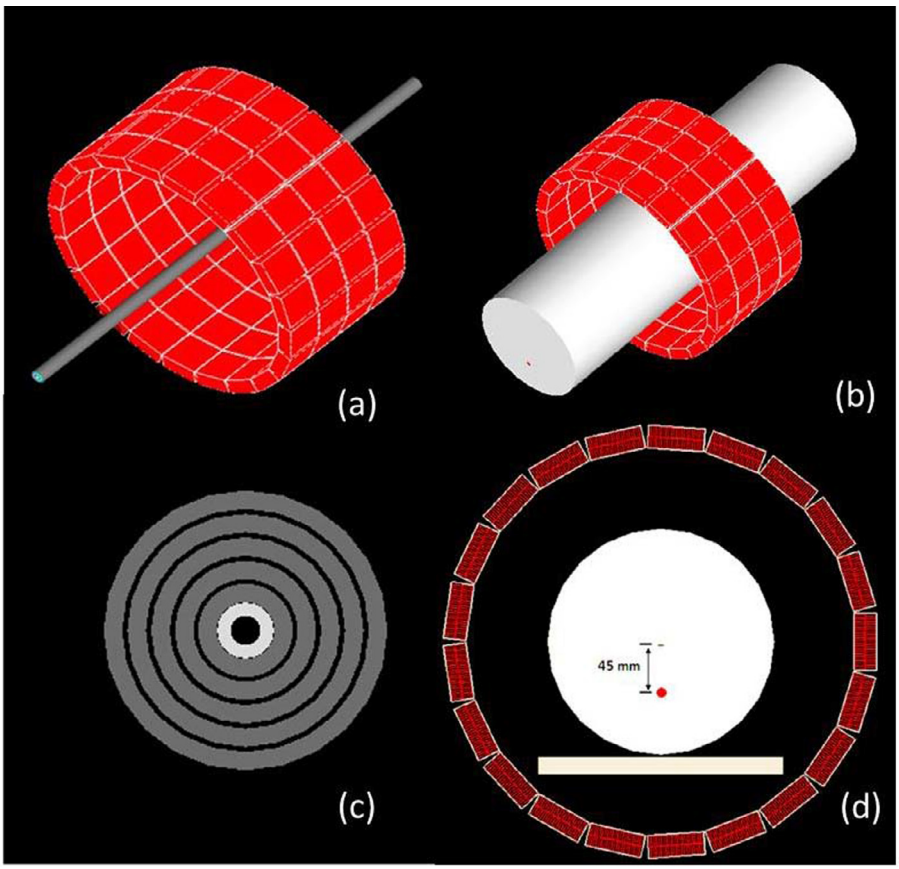

Fig. 3. (a) Side view of the simulated NeuroPET with NEMA sensitivity phantom; (b) side view of simulated NeuroPET with NEMA scatter phantom. (c) Cross-sectional view of five layers of the aluminum NEMA sensitivity phantom; (d) cross-sectional view of the simulated NeuroPET with NEMA scatter phantom along with the patient bed.

diameters of 6.4, 9.5, 12.7, 15.9, and 19.1 mm and a fixed wall thickness were also simulated (see Fig. 3a and c).

Similar to the manufacturer's data sheet, an energy threshold of 350 keV with a 7-ns coincidence window, and an MRD equal to the AFOV were selected (acquisition mode A). A total of 2.7 MBq activity was used with an acquisition time of 10 s. Source activity was sufficiently low to minimize the effects of dead-time and random events. The first simulation was performed with only the first aluminum tube in place. One aluminum tube was added per subsequent measurement. In addition, the count rate was normalized to that of the 70-cm line source. Finally, the sensitivity as a function of the total thickness of the aluminum sleeves was plotted and then extrapolated to an attenuation-free sensitivity value. This simulation was also repeated with the line sources placed at the FOV according to published experimental results, with a 400–650 keV energy window, and an MRD equal to half of the AFOV (acquisition mode B).

NECR: We modeled a 700-mm-long plastic tube with a 3.2-mm diameter placed in a polyethylene scatter phantom. While the phantom was positioned in the FOV center, the 700-mm F-18 line source was placed 45 mm below the transverse center (see Fig. 3b and 3 d). NECR was calculated for different activity values. It is noteworthy that we also simulated a patient bed that is used to hold the phantom in FOV.

2.3. Inter detector scattering evaluation

For quantification of IDS in the NeuroPET scanner, a 511 keV gamma-ray point source with 10 μCi activity was placed in the FOV center. To evaluate the crystal scattering in the detector blocks, no attenuating material was placed between the source and the detector blocks. The scatter events from the phantom were not taken into account. Optical photon transport was not implemented. We used GATE's ASCII output, which is basically a "hit" file. While complete photon history from the first interaction until absorption in the crystal can be extracted, we only used the first interaction location and the final absorbed location as relevant information to evaluate mis-positioned events.

With our in-house developed MATLAB code, we evaluated the characteristics of every interaction in the "hit" files and determined the fraction of mis-positioned events. Given the dual crystal layer configuration of the NeuroPET scanner, we defined two IDS event categories: cross-layer crystal scattering (CLCS), and inter-layer crystal scattering (ILCS). In the work published by Gu et al., they developed a LYSO-BGO single detector with dual-layer configuration and presented a CLCS algorithm to analyze their detector [17]. In this study, we modified their algorithm to examine LYSO-based DLO detectors in the full ring NeuroPET scanner and analyzed both CLCS and ILCS events. The detected singles events can be categorized as follows:

L1: The gamma photon deposits all its energy in the inner layer only.
L2: The gamma photon deposits all its energy in the outer layer only.
L1S: The gamma photon deposits its energy in the inner layer, but in a crystal other than the one with which it interacted.
L2S: The gamma photon deposits its energy in the outer layer, but in a crystal other than the one with which it interacted.
C1: The gamma photon interacts in both layers. The first interaction occurs in the inner layer, and its deposited energy in the inner layer is smaller than the outer layer.

C2: The gamma photon interacts in both layers. The first interaction occurs in the inner layer, and its deposited energy in the inner layer is larger than the outer layer.
C3: The gamma photon interacts in both layers. The first interaction occurs in the outer layer, and its deposited energy in the outer layer is smaller than the inner layer.
C4: The gamma photon interacts in both layers. The first interaction occurs in the outer layer, and its deposited energy in the outer layer is larger than the inner layer.

Fig. 4 shows all the above-mentioned event types. We calculated the fraction of each event type from the total number of interacting gamma rays. L1S and L2S determine the ILCS fraction, and C1 to C4 determine CLCS value. A total mis-positioned event was calculated by summing CLCS and ILCS.

3. Results

3.1. Validation study

Overall robustness verification: To verify our model, the accuracy of axial sensitivity (3D) and transaxial detection position were checked. Fig. 5(a) illustrates a histogram of the coordinates of the detected events corresponding to the gamma-ray interaction positions in the detector blocks. The scanner diameter of this histogram shows 357 mm, which matches our modeled scanner. Fig. 5(b) shows the simulated axial sensitivity (3D) of the NeuroPET. As expected, the system sensitivity peaks at the FOV center and then sharply decreases as the source moves towards the FOV periphery. System sensitivity goes to zero outside the axial FOV. The axial distance in the base of this distribution shows 220 mm, which is the same value as that of the axial FOV of the simulated scanner.

Point source sensitivity: The absolute sensitivity is defined as the ratio of total coincidence rate to the point source activity. Our results show an 8.2% point source sensitivity, which is 2.5% greater than that of the reported experimental results of ~8% [11].

NEMA line source sensitivity: Fig. 6 shows the simulation results of sensitivity measurements in the two acquisition modes, A and B, as a function of accumulated aluminum sleeve thickness. For MRD equal to half of the AFOV and a 400–650 keV energy window, we calculated a 7.81 kcps/MBq sensitivity compared with the reported 7.5 kcps/MBq. This value increased to 14.90 kcps/MBq (versus 14.5 kcps/MBq reported by the manufacturer) when MRD was equal to the AFOV, and only a 350 keV lower energy threshold was used. Therefore, the differences between the simulation and the experimental values [11,12] of the two acquisition modes are 4.1 and 2.7%.

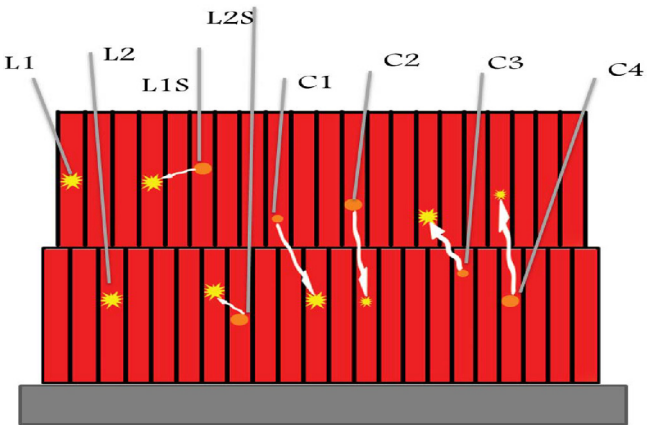

Fig. 4. Representation of different types of events in the NeuroPET detector. L1 (inner layer events), L2 (outer layer events), L1S (inner layer scattering events), L2S (outer layer scattering events), and C1–C4 (four types of cross layer crystal scattering (CLCS) events).

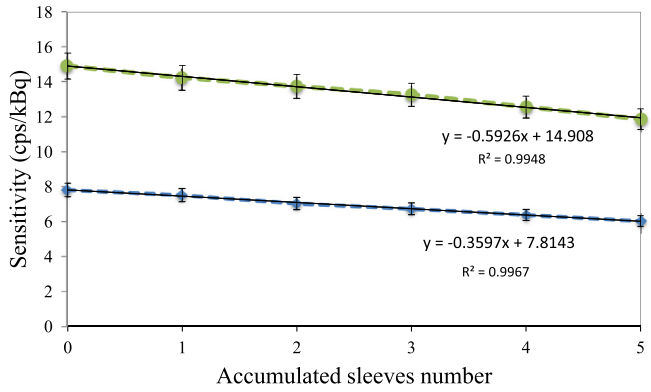

Fig. 6. Sensitivity as a function of aluminum sleeve thickness for two different data acquisition modes using NEMA-like line source.

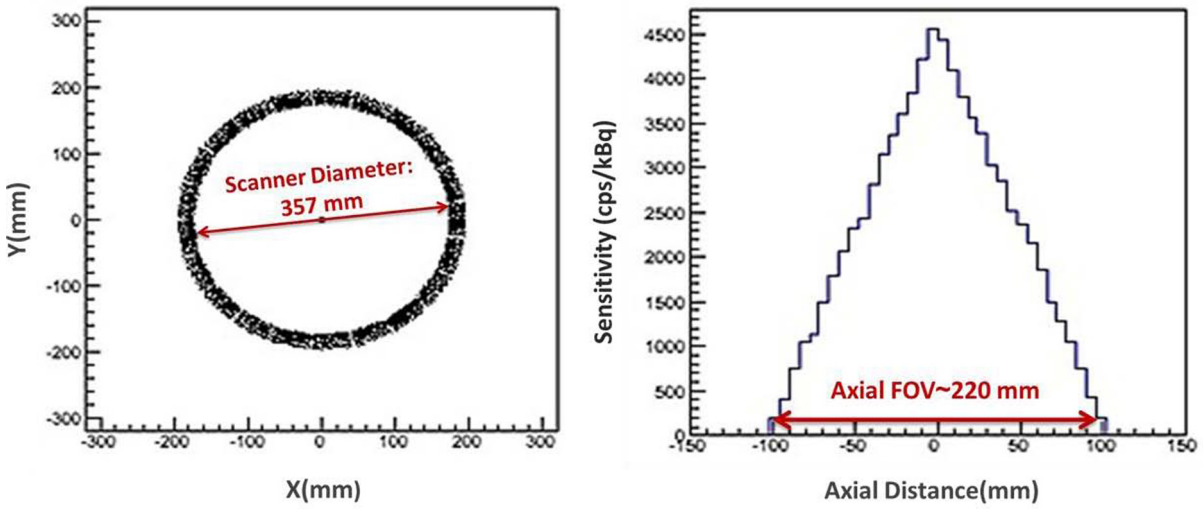

Fig. 5. (a) The NeuroPET transaxial detection position in the x–y plane. (b) The simulated NeuroPET sensitivity result as a function of axial position.

Noise equivalent count rate: The noise equivalent count rate without random subtraction is calculated using:

$$NECR_{1R} = \frac{T^2}{T+S+R} \quad (1)$$

where T, S, and R are the true, scatter, and random count rates, respectively. Fig. 7 shows a simulated NECR curve for a uniformly distributed activity concentration using the NEMA-NU 2007 scatter phantom. As marked in the figure: 20.3, 28.2, 36.7, and 38 kcps are obtained for activity concentrations of 1, 2, 3, and 6 kBq/ml, respectively. Additionally, a maximum NECR of 40.1 kcps is obtained for an activity of 3.7 kBq/ml, whereas the experimental results reported 38 kcps for the same activity concentration. The simulated NECR values show good agreement with the experimental data.

3.2. Inter-detector scatters

CLCS results: The fractions of different CLCS types are summarized in Table 1. The results show that the contributions of L1 (inner layer) and L2 (outer layer) are 67.5% and 30.5%, respectively. Additionally, the fraction of single events that interacted in both layers and are categorized as CLCS mis-positioned events is 1.98%. This value rises to approximately 4% in the coincidence mode. The C1 and C3 event types that account for up to 90% of the total CLCS mis-positioned events deposit most of their energy in different layers than the first interaction layer. The results also show that with ~80% share, C1 events significantly contribute to the total CLCS events, therefore, much attention should be paid to identifying and eliminating this event type.

ILCS results: The results of ILCS are summarized in Table 2. For clarification, we define ILCS using the following:

$$L1S\% = \frac{L1S}{L1} \times 100$$

$$L2S\% = \frac{L2S}{L2} \times 100$$

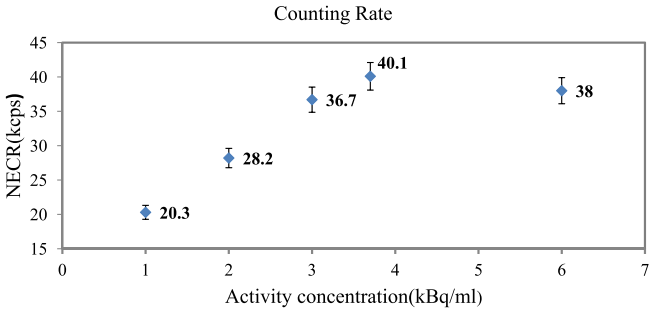

Fig. 7. The noise equivalent count rate (NECR) against activity concentration for the NeuroPET.

$$ILCS = \frac{(L1S + L2S)}{total\ number\ of\ interacting\ gammas}$$

Table 2 shows that the percentages of single events detected as L1S% (crystal scatter fraction in the inner layer) and L2S% (crystal scatter fraction in the outer layer) are 8.0% and 7.3%, respectively. The total fraction of single events that are detected as ILCS mis-positioned events is 7.68%. This fraction will increase to approximately 16% in coincidence mode. It should be noted that according to the results, the probabilities of L1S and L2S events are almost the same.

Total inter detector scattering results by summing CLCS and ILCS we arrive at 9.66%, which represents a value for all mis-positioned events to the total interacted photons (L1 + L2 + C1 + C2 + C3 + C4).

4. Discussion and conclusion

In the overall robustness verification of the MC system model, by checking the accuracy of axial sensitivity (3D) and transaxial detection position in Fig. 5(a), we observed that the distribution is completely homogeneous and isotropic. Additionally, the ring diameter in this distribution equals our modeled scanner so that all detectors are positioned and simulated correctly.

In the validation study of the MC system model, the results of the point- and line-source sensitivity (Fig. 6) indicate an overestimation of 2.5% for the point source and 4.1% and 2.7% for two acquisition modes using the line source when compared with the measured experimental data. This overestimation is expected because the actual detector signal processing chain, which is not exactly modeled here, includes block non-uniform energy resolutions, light transport, light leakage, and SiPM, as well as optical coupling efficiencies.

The simulated values of the NECR show good agreement with the experimental results [11,12]. In this analysis, due to time-consuming simulation runs, we only evaluated 5 source activities. However, the NECR curve is acceptable, and its peak matches well with the experimental data. Generally, the small deviations at high activity levels are due to the deficiency of GATE code in simulating the complicated behavior of electronic systems. Indeed, the developed GATE model is an approximation and is based on limited detail on geometric information and the actual detector signal processing chain. Nevertheless, the simulated results, especially in low activity levels, agree well with the measured data.

Among CLCS results, we found that C1 contributes to a larger fraction of events. This behavior is quite compatible with the work performed by Gu et al. [17], and this is due to Compton kinematics. We know that in Compton scattering, gamma rays preferentially scatter in the forward direction and deposit smaller amounts of energy in the first interaction crystal. This is quite compatible with other studies [17,30]. When we compare our results quantitatively with those of Gu et al., we observe that our measured value for C1 events is smaller than their result. In addition, the total CLCS mis-positioned errors is smaller than what they reported. This differ-

Table 1
The fractions of different types of CLCS events.

Type	L1	L2	C1	C2	C3	C4	Cross layer mis-positioned events
Fraction	67.5%	30.5%	1.6%	0.03%	0.24%	0.12%	1.98%

Table 2
The fractions of different types of ILCS events.

Type	L1%	L2%	L1S%	L2S%	Inter layer mis-positioned events
Fraction	67.5%	30.5%	8.05%	7.35%	7.68%

ence may be explained by the number of detector rings, as our model is based on a 4-ring (and 21 blocks per ring) detector system in which some annihilation photons can obliquely interact with the detectors, while in their report, only a single detector with gamma rays traveling in the forward direction was modeled. This could lead to a decrease in the CLCS mis-positioned errors but to an increase in ILCS errors. Finally, for restoration of CLCS errors, we should focus more on C1 with the extraction of inner layer signal components separately from those of the outer layer.

By comparing the values in Table 2, we observe that the fraction of crystal scattering in the inner layer (8.05%) is approximately equal to that of the outer layer (7.35%) within one standard deviation. This is because the two crystal layers have same specifications such as crystal type and geometry.

Comparing the ILCS and CLCS values shows that ILCS mis-positioned errors are very significant (7.68% versus 1.98% in single events, and 16% versus 4% in coincidence mode), corresponding to 79% of the total mis-positioned errors. Therefore, it is important to seek solutions to reduce ILCS mis-positioning errors to improve image spatial resolution and SNR. As previously stated, there are algorithms that are based on Compton kinematics and the maximum signal to identify the first location of gamma ray interactions to minimize the effect of IDS on image quality.

We modeled the NeuroPET scanner mainly due to its practical design, which is based on conventional and available detector components, single-side readout, and mobility. The developed and validated model can provide a reliable tool for our detector development research and will be used as a guide to understand the pros and cons of new detector designs featuring different geometries, including staggered layers, as well as those with different scintillator materials.

Acknowledgment

This work was supported under grant number 28203, Tehran University of Medical Sciences, Tehran, Iran.

References

[1] Zaidi H, Montandon M-L. The new challenges of brain PET imaging technology. Curr Med Imaging Rev 2006;2:3–13.
[2] Wienhard K, Schmand M, Casey M, Baker K, Bao J, Eriksson L, et al. The ECAT HRRT: performance and first clinical application of the new high resolution research tomograph. IEEE Trans Nucl Sci 2002;49:104–10.
[3] Watanabe M, Shimizu K, Omura T, Takahashi M, Kosugi T, Yoshikawa E, et al. A new high resolution PET scanner dedicated to brain research. In: IEEE Nucl Sci Symp Conf Rec. IEEE; 2001. p. 1218–22.
[4] Karp JS, Surti S, Daube-Witherspoon ME, Freifelder R, Cardi CA, Adam L-E, et al. Performance of a brain PET camera based on anger-logic gadolinium oxyorthosilicate detectors. J Nucl Med 2003;44:1340–9.
[5] Braem A, Llatas MC, Chesi E, Correia J, Garibaldi F, Joram C, et al. Feasibility of a novel design of high resolution parallax-free Compton enhanced PET scanner dedicated to brain research. All the authors are members of the CIMA Collaboration. Phys Med Biol 2004;49:2547.
[6] Yamaya T, Yoshida E, Obi T, Ito H, Yoshikawa K, Murayama H. First human brain imaging by the jPET-D4 prototype with a pre-computed system matrix. IEEE Trans Nucl Sci 2008;55:2482–92.
[7] Kinahan P, Majewski S, Elston B, Harrison R, Qi J, Manjeshwar R, et al. Design considerations for AMPET: the ambulatory micro-dose, wearable PET brain imager. J Nucl Med 2015;56:1540.
[8] González AJ, Majewski S, Sánchez F, Aussenhofer S, Aguilar A, Conde P, et al. The MINDView brain PET detector, feasibility study based on SiPM arrays. Nucl Instrum Methods Phys Res A 2016;818:82–90.
[9] Wang Z, Yu W, Xie S. A dedicated PET system for human brain and head/neck imaging. In: IEEE Nucl Sci Symp Conf Rec. IEEE; 2013. p. 1–4.
[10] The TRIMAGE project[Internet]. Available from: <http://www.trimage.eu/>.
[11] NeuroPET/CT. The World's First Portable PET/CT [Datasheet]. Photo Diagnostic Systems Inc.; 08.08.2012 [Available from: <http://www.photodiagnostic.com/>.
[12] Grogg K, Toole T, Ouyang J, Zhu X, Normandin MM, Johnson K, et al. NEMA and clinical evaluation of a novel brain PET-CT scanner. J Nucl Med 2015. http://dx.doi.org/10.2967/jnumed.115.159723.
[13] Ouyang J, Toole T, Keeler M, Grogg K, Zhu X, Li Q. Performance comparison between NeuroPET-CT and Siemens ECAT HR+: NEMA and patient studies. J Nucl Med 2014;55:2162.
[14] Stortz G, Walker M, Thompson C, Goertzen A, Retiere F, Zhang X, et al. Characterization of a new MR compatible small animal PET scanner using Monte-Carlo simulations. IEEE Trans Nucl Sci 2013;60:1637–44.
[15] Zhang X, Stortz G, Sossi V, Thompson CJ, Retière F, Kozlowski P, et al. Development and evaluation of a LOR-based image reconstruction with 3D system response modeling for a PET insert with dual-layer offset crystal design. Phys Med Biol 2013;58:8379.
[16] Gu Y, Pratx G, Lau FW, Levin CS. Effects of multiple-interaction photon events in a high-resolution PET system that uses 3-D positioning detectors. Med Phys 2010;37:5494–508.
[17] Gu Z, Prout D, Silverman R, Herman H, Dooraghi A, Chatziioannou A. A DOI, detector with crystal scatter identification capability for high sensitivity and high spatial resolution PET imaging. IEEE Trans Nucl Sci 2015;62:740–7.
[18] Comanor K, Virador P, Moses W. Algorithms to identify detector Compton scatter in PET modules. IEEE Trans Nucl Sci 1996;43:2213–8.
[19] Ito M, Lee MS, Lee JS. Continuous depth-of-interaction measurement in a single-layer pixelated crystal array using a single-ended readout. Phys Med Biol 2013;58:1269.
[20] Sitek A, Andreyev A. Detector response correction for 3D PET using Bayesian modeling of the location of interaction. In: IEEE Nucl Sci Symp Conf Rec. IEEE; 2012. p. 2348–50.
[21] Pedemonte S, Pierce L, Van Leemput K. A machine learning method for fast and accurate characterization of depth-of-interaction gamma cameras. Biol: Phys. Med; 2017.
[22] Ito M, Hong SJ, Lee JS. Positron emission tomography (PET) detectors with depth-of-interaction (DOI) capability. Biomed Eng Lett 2011;1:70–81.
[23] Jan S, Santin G, Strul D, Staelens S, Assie K, Autret D, et al. GATE: a simulation toolkit for PET and SPECT. Phys Med Biol 2004;49:4543.
[24] Agostinelli S, Allison J, Ka Amako, Apostolakis J, Araujo H, Arce P, et al. Geant4—a simulation toolkit. Nucl Instrum Methods Phys Res A 2003;506:250–303.
[25] Karakatsanis N, Sakellios N, Tsantilas N, Dikaios N, Tsoumpas C, Lazaro D, et al. Comparative evaluation of two commercial PET scanners, ECAT EXACT HR + and Biograph 2, using GATE. Nucl Instrum Methods Phys Res A 2006;569:368–72.
[26] Schmidtlein CR, Kirov AS, Nehmeh SA, Erdi YE, Humm JL, Amols HI, et al. Validation of GATE Monte Carlo simulations of the GE Advance/Discovery LS PET scanners. Med Phys 2006;33:198–208.
[27] Geramifar P, Ay M, Zafarghandi MS, Sarkar S, Loudos G, Rahmim A. Investigation of time-of-flight benefits in an LYSO-based PET/CT scanner: a Monte Carlo study using GATE. Nucl Instrum Methods Phys Res A 2011;641:121–7.
[28] Zeraatkar N, Ay MR, Kamali-Asl A, Zaidi H. Accurate Monte Carlo modeling and performance assessment of the X-PET™ subsystem of the FLEX Triumph™ preclinical PET/CT scanner. Med Phys 2011;38:1217–25.
[29] Association NEM. NEMA standards publication NU 2-2007: performance measurements of positron emission tomographs. National Electrical Manufacturers Association; 2007.
[30] Vaska P, Stoll SP, Woody CL, Schlyer DJ, Shokouhi S. Effects of intercrystal crosstalk on multielement LSO/APD PET detectors. IEEE Trans Nucl Sci 2003;50:362–6.